Fluorescence lifetime imaging for explosive detection

Andrew B. Matheson,[1],* **Edward B. Ogugu,[2]** **Ross N. Gillanders,[2]** **Graham A. Turnbull,[2]** **and Robert Henderson[1]**

[1]*School of Engineering, Institute for Integrated Micro and Nano Systems, University of Edinburgh, Edinburgh EH9 3FF, United Kingdom*
[2]*Organic Semiconductor Centre, School of Physics and Astronomy, University of St Andrews, St Andrews, Fife, KY16 9SS, United Kingdom*
*a.matheson@ed.ac.uk

In this Letter, a time-resolved 120×128 pixel single-photon avalanche diode (SPAD) sensor is used in conjunction with an array of organic semiconductor films as a means of detecting the presence of explosive vapors. Using the spatial and temporal resolution of the sensor, both fluorescence intensity and fluorescence lifetime can be monitored on a pixel-by-pixel basis for each of the polymer films arranged in a 2×2 grid. This represents a significant improvement on similar systems demonstrated in the past, which either offer spatial resolution without the temporal resolution required to monitor lifetime or offer only a single bulk measurement of lifetime and intensity without the spatial resolution. The potential of the sensing system is demonstrated using vapors of DNT, and differing responses for each of the four polymer films is observed. This system has clear applications as the basis of a portable chemical fingerprinting tool with applications in humanitarian demining and security.

Fluorescence lifetime imaging is the imaging modality whereby a contrast is provided not just by fluorescence intensity but by the characteristic lifetime of the fluorescence decay. Although largely employed as part of fluorescence lifetime imaging microscopy (FLIM), there are also applications for wide-field fluorescence lifetime imaging (WFLIm). Single-photon avalanche diode (SPAD) arrays are increasingly being employed for WFLIm, due to their high sensitivity, low noise, small footprint, and the fact that sub-ns timing electronics can be integrated directly into each pixel [1]. To date, the applications of FLIM and WFLIm have largely been focused on biological and biomedical systems [2–9], but fluorescence lifetime may also be used as a tool to measure photo-physical and chemical processes in materials such as organic and organometallic semiconductors [10,11].

One application of organic semiconductors is in humanitarian demining, where interactions with nitroaromatic molecules contained in the vapor emitted from landmines result in a quenching of fluorescence intensity and a change in fluorescence lifetime [12]. Correctly identifying explosives from an improvised explosive device (IED) in a complex environment can be challenging, but previously it has been shown that a system based on a small time-resolved SPAD array may be an effective and portable tool for explosive sensing [13]. Using the time resolution of the SPAD pixels to monitor both lifetime and intensity gives an additional parameter, which may be used to help classify the response of a given semiconductor film to a specific vapor. Additionally, when monitoring fluorescence using a standard CMOS sensor, photo-diode, or CCD [14,15], it can be difficult to decouple changes in intensity from fluctuations in pump power. The fluorescence lifetime however should be broadly independent of the excitation intensity. In the previously described system, a small array of 4×16 SPADs was used, with all 64 SPADs summed together to give a single response, thus losing spatial information [13]. Using the spatial resolution of a SPAD sensor with thousands of pixels to monitor the response of *multiple* different organic semiconductor films simultaneously should thus give a more specific response and allow for rapid chemical fingerprinting [16].

In recent years, SPAD technology has developed significantly—SPADs are more sensitive and may be combined in a larger number of pixels than ever before. In this work a miniaturized SPAD sensor array is employed to perform WFLIm on multiple polymers simultaneously. The Endocam sensor is a 120×128 pixel time-resolved SPAD array described in some detail in Refs. [17–19]. It achieves time resolution via the application of a 0.379 ns time gate to the photon counting electronics, which may be moved in 0.379 ns steps relative to an excitation laser pulse. For the work described hereafter, laser excitation was provided by a Picoquant PDL 800-B driving a 379 nm pulse laser diode (100 ps pulse duration), which was synchronized to an FPGA controller generating a master clock for the system.

A schematic of the optical layout of the system is shown in Fig. 1(a). The excitation beam enters the sealed sample chamber through a window on the front and illuminates the polymer array. The polymer array is angled at approximately 45° to both this excitation window on the front of the chamber and the emission window on the side of the chamber. Fluorescence emitted through the emission window then passes through a long pass filter (Thorlabs, 400 nm cut on) and is collected by a lens mounted on the Endocam to form an image.
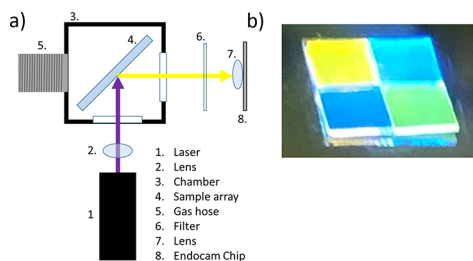
Fig. 1. (a) Schematic diagram of the system. (b) Array of (clockwise from top left) SY, PFO, $F8_{0.9}BT_{0.1}$, and PFDD, under UV illumination.

The fluorescent polymer array (see Fig. 1(b)) consists of a 2×2 grid of Super Yellow (SY); poly[9,9-dioctylfluorenyl-2,7-diyl] (PFO); poly[9,9-didodecylfluorenyl-2,7-diyl] (PFDD); and poly[(9,9-dioctylfluorenyl-2,7-diyl)-co-(1,4-benzo-[2,1,3]-thiadiazole)] with 10% benzothiadiazole units ($F8_{0.9}BT_{0.1}$). SY was obtained from Sigma-Aldrich Ltd., while PFO, PFDD, and $F8_{0.9}BT_{0.1}$ were obtained from the American Dye Source Inc. Each polymer exhibits a distinct response to the presence of nitroaromatic vapors, due to different electronic energy levels and non-covalent binding interactions with the analyte, and the nature of this response will depend on the specific analyte. Endocam was controlled via a MATLAB interface as described in Ref. [19]. The chip can operate in a rapid lifetime determination (RLD) mode at frame rates of up to ~7 Hz [18], but to allow full decays to be analyzed in the post processing, it was used here in a sliding gate mode to obtain data at 31 gate positions (a time range of ~12 ns). The fluorescence lifetime was calculated in real time by performing a least squares fit to the linearized data on a pixel-by-pixel basis to return a single characteristic lifetime per pixel per image, to generate WFLIm images with a frame rate of 0.3 Hz. The IRF of the sensor has previously been measured as 0.55 ns [18].

To establish a stable baseline measurement, the fluorescence lifetime was initially monitored, while the array was exposed to a clean nitrogen carrier gas at a flow rate of 6 L/min. Successive WFLIm images were obtained by sweeping the time gate in the manner described earlier. Figure 2 shows the fluorescence decay curves for each of the films for this baseline measurement,
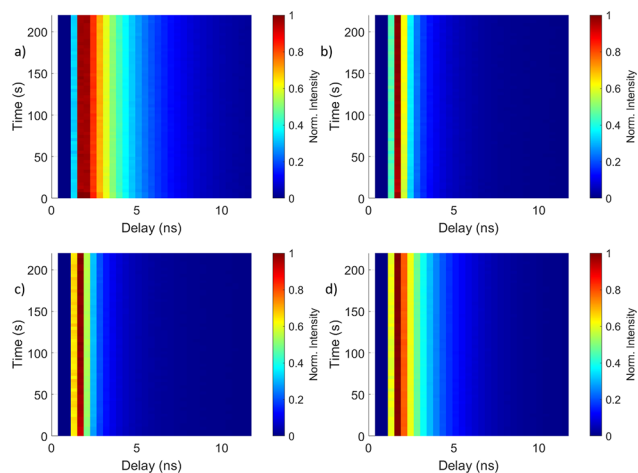
Fig. 2. Normalized fluorescence intensity as a function of time delay in ns and time in seconds of nitrogen exposure, for (a) $F8_{0.9}BT_{0.1}$, (b) PFO, (c) PFDD, and (d) SY.
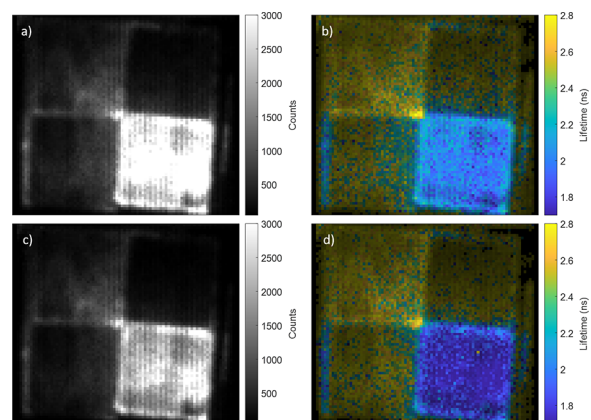

Fig. 3. (a) (c) Intensity and (b) (d) WFLIm images of an array of (clockwise from top left) $F8_{0.9}BT_{0.1}$, PFO, SY, and PFDD. Top-row images were obtained on the initial exposure to N2 and bottom row following 72 s of exposure to the DNT.

produced by summing together the pixels corresponding to each quadrant of the polymer array. The horizontal delay axis represents the position of the active time bin in ns relative to the master clock, with the laser excitation pulse arriving at ~1 ns. The vertical time axis represents the amount of time elapsed from the beginning of the experiment in seconds. The change in intensity along the horizontal axis is due to the characteristic lifetime of the fluorescence decay for each film and remains consistent, but the vertical time axis shows no significant change over >3 min of nitrogen exposure for any of the films.

Having established a stable baseline, the films were next exposed to vapor flow of DNT (a decay product of TNT) of concentration well below its saturated vapor pressure of 400 ppb. The experiment consisted of a cycle of 40 s of clean nitrogen flow, then ~70 s of exposure to the DNT vapor in the nitrogen carrier gas, and then 100 s of purge in clean nitrogen. Figure 3 shows both intensity [(a) and (c)] and WFLIm [(b) and (d)] images taken from the polymer test array, before and after the DNT vapor exposure, respectively. Images such as those shown in Fig. 3 are generated in real time during the measurement and shown on the GUI, giving a rapid visual indication of the presence of any fluorescence quenching. Thus, we can observe that the sensor not only allows us to monitor four films simultaneously but to observe a distribution of lifetimes on a single film.

To illustrate this, Fig. 4 shows histograms corresponding to each of the four polymers. Before estimating lifetime (using the same linearized mono-exponential fit employed via the GUI in real time), a 2×2 pixel binning is performed to improve SNR. Following exposure to the DNT vapor, the SY film shows a clear shift in the lifetime distribution. $F8_{0.9}BT_{0.1}$ has no significant change in the distribution, while PFO and PFDD show an apparent increase in pixels returning longer lifetimes. We believe this increase is actually a consequence of the reduced photon count approaching the measurement noise floor. To improve signal to noise, we may also sum multiple pixels for each polymer, as shown in Fig. 5. We observe that the fluorescence intensity and lifetime of each of the four films are stable during the first 40 s (when exposed to only nitrogen) and match the pulsed fluorescence dynamics of the baseline measurement. On exposure to DNT vapor (times after the white-dashed line), however, each of the four films shows a more rapid decay of the
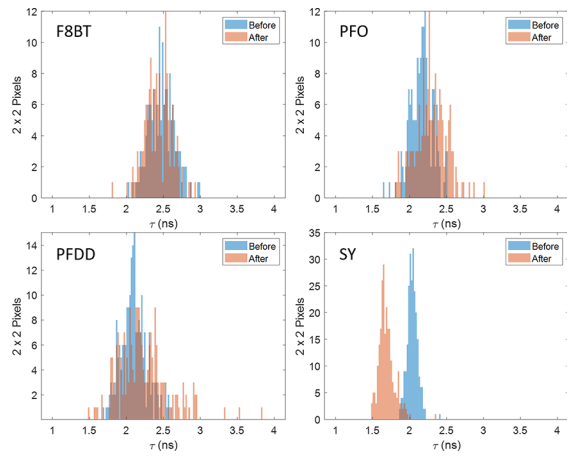
Fig. 4. Histograms of lifetime calculated using a linearized mono-exponential fit before (blue) and after (pink) exposure to DNT. The y axis is the number of blocks of 2×2 pixels (produced by spatially binning by a factor of 2) for each given lifetime.
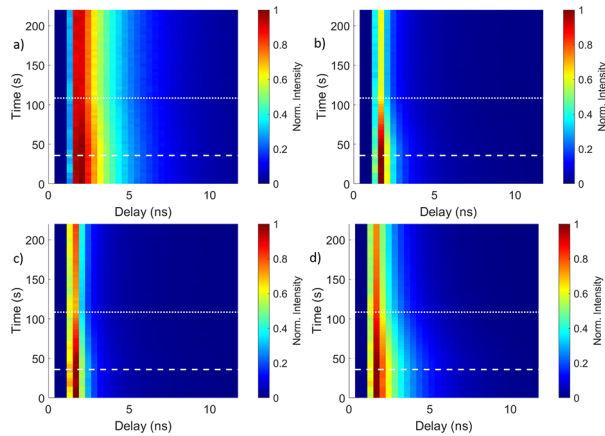
Fig. 5. Normalized fluorescence intensity as a function of time delay in ns and time in seconds for (a) $F8_{0.9}BT_{0.1}$, (b) PFO, (c) PFDD, and (d) SY. White dashed lines represent the time DNT vapor is introduced to the sample chamber, and white dotted lines represent the time the DNT flow is turned off and the clean nitrogen is reintroduced.

fluorescence intensity with delay, most obviously for the SY emission. This change is indicative of fluorescence quenching due to absorption of DNT molecules in the film. Interestingly, the peak intensity also falls on exposure to DNT, an indication that there is a rapid quenching occurring on a time scale shorter than the instrument IRF. The extent of this reduction varies for each material, with PFO showing the largest fall in the peak intensity.

It is also possible to calculate the integrated intensity over the full ~12 ns delay window for each time step, which is plotted in Fig. 6(a), providing the information one would obtain in a steady-state fluorescence measurement. We find that the integrated intensity of each of the films is initially stable during the clean nitrogen flow and then falls on an extended exposure to DNT. The extent of this fluorescence quenching differs for each film, with SY and PFO showing the greatest degree of fluorescence quenching during ~70 s of the DNT exposure between ~40 s and ~110 s. When the materials are purged with
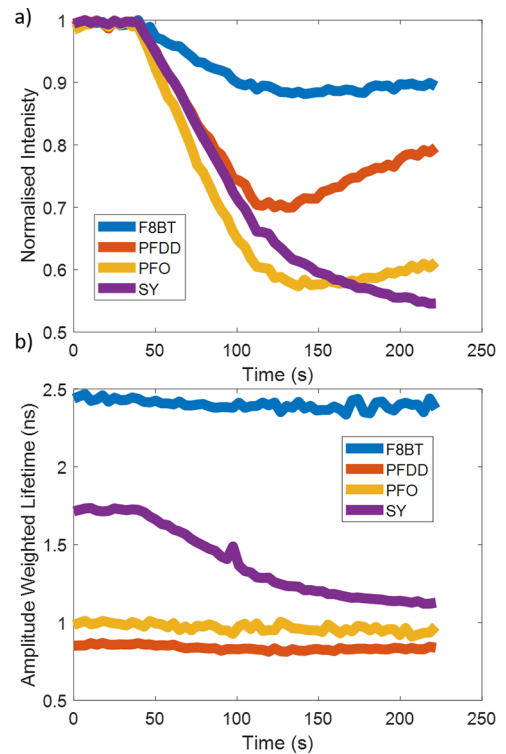
Fig. 6. (a) Normalized integrated intensity and (b) amplitude-weighted effective lifetime as a function of time for each of the films.

clean nitrogen after 110 s, we find that the fluorescence intensity of $F8_{0.9}BT_{0.1}$, PFO, and PFDD shows recovery (of varying strengths), but the intensity of SY continues to decrease. This would suggest that molecular binding to DNT is stronger for SY than the other polymers and that there may be a continued slow diffusion of DNT deeper into the film.

As mentioned previously, for real-time acquisition, the logarithm of the intensity for each pixel was obtained, and a linear fit was performed to return an approximate lifetime, as shown in Figs. 3 and 4. This is a useful way of rapidly monitoring changes in lifetime; however the actual fluorescence dynamics of the films are generally multi-exponential decays. Such complex dynamics arise as some of the polymers exhibit a bi-exponential fluorescence decay in pristine solid films, while the DNT-induced quenching adds a further process depleting the excited state population. To more accurately describe the decay dynamics of each of the films during the full delay window, a tri-exponential decay

$$I = A_1 \exp\left(-\frac{t}{\tau_1}\right) + A_2 \exp\left(-\frac{t}{\tau_2}\right) + A_1 \exp\left(-\frac{t}{\tau_3}\right) \quad (1)$$

is required for each time step. An amplitude-weighted lifetime τ may be calculated from Eq. (1) using Eq. (2):

$$\tau = \frac{\tau_1 A_1 + \tau_2 A_2 + \tau_3 A_3}{A_1 + A_2 + A_3}. \quad (2)$$

While a more detailed study of the dynamics would use the individual decay rates and amplitudes, $\langle \tau \rangle$ may be easily plotted for each material. Figure 6(b) shows a comparison of the changes in $\langle \tau \rangle$ for each film with time. Note that the values of $\langle \tau \rangle$ obtained via Eq. (2) differ from the real-time linearized

fits shown in Figs. 3 and 4, as they better represent the spatially averaged fluorescence decays. $F8_{0.9}BT_{0.1}$ and SY show changes in normalized lifetime, which largely follow the form of changes in the intensity they exhibit; $F8_{0.9}BT_{0.1}$ shows a weak quenching, followed by a small recovery, whereas SY shows a significant quenching initially, which continues even after the DNT flow is stopped. The fractional change in $F8_{0.9}BT_{0.1}$ lifetime is very small compared to the intensity change, indicating that the majority of quenching in $F8_{0.9}BT_{0.1}$ occurs on a time scale much faster than the 0.379 ns time gate. PFO and PFDD show a very similar dynamics to each other, with much less change in their amplitude-weighted lifetime than in intensity. The similarity between the two is not surprising given the only difference in their chemical structure is the length of their side chains (8 and 12 carbons, respectively). The greater change in intensity than in lifetime is consistent with the previously noted high degree of fast quenching of these materials, leading to a fast component, which is not being fully resolved but is evident in the fall in the peak intensity.

Using the information contained in Figs. 3–6, it is possible to construct a distinctive profile of how fluorescence of the organic semiconductor array changes in the presence of DNT: fluorescence quenching is observed for all four polymers, although this is fairly weak for $F8_{0.9}BT_{0.1}$. While fluorescence quenching of SY by DNT is accompanied by a clear reduction in the lifetime, PFO and PFDD appear to be quenched on a very short time scale, based on the different changes in the time-integrated fluorescence and the average lifetime. On purging the array with clean nitrogen, there is a recovery in the intensity of PFO, PFDD, and $F8_{0.9}BT_{0.1}$, while for SY, both the intensity and lifetime continue to decrease (as the retained DNT may penetrate deeper into the film). This rich information obtained by using an imaging system with both spatial and temporal resolution provides an insight to the nature of the quenching and molecular binding processes and offers a route to build a library of nitroaromatic responses. Having demonstrated the capabilities for this system using a single nitroaromatic, future works will develop a fingerprint classification for a range of different chemicals; both explosives and their by-products and distractants may be encountered in the environment, eventually building a library of polymer/vapor responses.

This proof-of-concept demonstration is a benchtop system, but it has been shown previously that SPADs can be packaged in the robust systems suitable for use in the field [13]. Given that Endocam has a very small footprint and the ability of the chip to operate at a distance from its control board, make it an especially suitable sensor for integration into a portable device for a remote detection of the explosives [19,20].

Disclosures. The authors declare no conflicts of interest.

Data availability. Data underlying the results presented in this paper are available in Ref. [21]. For the purpose of open access, the author has applied a Creative Commons Attribution (CC BY) license to any Author Accepted Manuscript version arising from this submission.

REFERENCES

1. I. Gyongy, T. Al Abbas, N. Finlayson, N. Johnston, N. Calder, A. Erdogan, N. Dutton, R. Walker, and R. Henderson, SPIE Emerging Imaging and Sensing Technologies for Security and Defence III **10799**, 1079907 (2018).
2. J. McGinty, N. P. Galletly, C. Dunsby, I. Munro, D. S. Elson, J. Requejo-Isidro, P. Cohen, R. Ahmad, A. Forsyth, A. V. Thillainayagam, M. A. A. Neil, P. M. W. French, and G. W. Stamp, Biomed. Opt. Express **1**, 627 (2010).
3. J. M. Paredes, M. D. Giron, M. J. Ruedas-Rama, A. Orte, L. Crovetto, E. M. Talavera, R. Salto, and J. M. Alvarez-Pez, J. Phys. Chem. B **117**, 8143 (2013).
4. J. Requejo-Isidro, J. McGinty, I. Munro, D. S. Elson, N. P. Galletly, M. J. Lever, M. A. A. Neil, G. W. H. Stamp, P. M. W. French, P. A. Kellett, J. D. Hares, and A. K. L. Dymoke-Bradshaw, Opt. Lett. **29**, 2249 (2004).
5. S. Cheng, R. M. Cuenca, B. Liu, B. H. Malik, J. M. Jabbour, K. C. Maitland, J. Wright, Y.-S. L. Cheng, and J. A. Jo, Biomed. Opt. Express **5**, 921 (2014).
6. H. Sparks, S. Warren, J. Guedes, N. Yoshida, T. C. Charn, N. Guerra, T. Tatla, C. Dunsby, and P. French, J. Biophotonics **8**, 168 (2015).
7. J. A. Jo, S. Cheng, R. Cuenca-Martinez, E. Duran-Sierra, B. Malik, B. Ahmed, K. Maitland, Y.-S. L. Cheng, J. Wright, and T. Reese, in 2018 40th Annual International Conference of the IEEE Engineering in Medicine and Biology Society (EMBC) (2018), pp. 3009–3012.
8. E. Duran-Sierra, S. Cheng, R. Cuenca-Martinez, B. Malik, K. C. Maitland, Y. S. Lisa Cheng, J. Wright, B. Ahmed, J. Ji, M. Martinez, M. Al-Khalil, H. Al-Enazi, and J. A. Jo, Oral Oncol. **105**, 104635 (2020).
9. J. E. Phipps, D. Gorpas, J. Unger, M. Darrow, R. J. Bold, and L. Marcu, Phys. Med. Biol. **63**, 015003 (2017).
10. J. Gu, Y. Gao, J. Wu, Q. Li, A. Li, W. Zhang, H. Dong, B. Wen, F. Gao, and Y. S. Zhao, ACS Appl. Mater. Interfaces **9**, 8891 (2017).
11. W. Min, S. Chuan-Xiang, Z. Chuang, and Y. Jiannian, J. Photonics Energy **8**, 032205 (2018).
12. R. N. Gillanders, J. M. E. Glackin, Z. Babić, M. Muštra, M. Simić, N. Kezić, G. A. Turnbull, and J. Filipi, Chemosphere **273**, 129646 (2021).
13. Y. Wang, B. R. Rae, R. K. Henderson, Z. Gong, J. Mckendry, E. Gu, M. D. Dawson, G. A. Turnbull, and I. D. W. Samuel, AIP Adv. **1**, 032115 (2011).
14. R. N. Gillanders, I. A. Campbell, F. Chen, P. O. Morawska, I. D. W. Samuel, and G. A. Turnbull, in 2016 4th International Conference on Photonics, Optics and Laser Technology (PHOTOPTICS) (2016), pp. 1–5.
15. R. N. Gillanders, I. D. W. Samuel, and G. A. Turnbull, Sens. Actuators, B **245**, 334 (2017).
16. N. Bolse, R. Eckstein, M. Schend, A. Habermehl, C. Eschenbaum, G. Hernandez-Sosa, and U. Lemmer, Flex. Print. Electron. **2**, 024001 (2017).
17. T. A. Abbas, O. Almer, S. W. Hutchings, A. T. Erdogan, I. Gyongy, N. A. W. Dutton, and R. K. Henderson, in 2019 Symposium on VLSI Circuits (2019), pp. C260–C261.
18. A. T. Erdogan, T. A. Abbas, N. Finlayson, C. Hopkinson, I. Gyongy, O. Almer, N. A. W. Dutton, and R. K. Henderson, IEEE J. Solid-State Circuits **57**, 1649 (2022).
19. A. Matheson, A. Erdogan, C. Hopkinson, S. Borrowman, G. Loake, M. Tanner, and R. K. Henderson, Opt. Express **31**, 22766 (2023).
20. D. Angelone, S. Konugolu Venkata Sekar, W. Messina, A. Matheson, A. Erdogan, R. Henderson, R. Burke, and S. Andersson-Engels, *Advanced Biomedical and Clinical Diagnostic and Surgical Guidance Systems XXI*, Vol. 12368 (SPIE, 2023).
21. E. Graham, J. Moss, N. Burton, Y. Roochun, C. Armit, and R. Baldock, "eHistology Kaufman Atlas Plate 22b image d," University of Edinburgh, College of Medicine and Veterinary Medicine, (2015).https://doi.org/10.7488/ds/7474.